Shocked Molecular Gas in the Supernova Remnants W 28 and W 44: Near-infrared and millimeter-wave observations

William T. Reach, Jeonghee Rho, and T. H. Jarrett

Infrared Processing and Analysis Center, California Institute of Technology, Pasadena, CA 91125

reach@ipac.caltech.edu

ABSTRACT

High resolution millimeter-wave (CO, CS, and HCO⁺ rotational lines) and near-infrared (H₂ 2.12 μ m rovibrational line, Fe II fine-structure line) observations of the supernova remnants W 28 and W 44 reveal extensive shocked molecular gas where supernova blast waves are propagating into giant molecular clouds. New CO observations were carried out with the IRAM 30-m and ARO 12-m telescopes, and the near-infrared observations were with Prime Focus Infrared Camera and Wide-Field Infrared Camera on the Palomar Hale 200-inch telescope. The near-infrared observations reveal shocked H₂ emission from both supernova remnants, showing intricate networks of filaments on arcsec scales, following the bright ridges of the radio shells. The emission is particularly bright in the northeastern, southern and western parts of W44 and the eastern bar in W28. The H₂ emission reveals some bright, clumpy structures as well as very thin filamentary structures likely to be individual shock fronts seen edge-on. The high-resolution IRAM CO(2-1) and CS(2-1) spectra clearly distinguish between the shocked and pre-shock gas for most of SNRs. Some of the CO spectra appear to have multiple components, but the less-optically-thick ¹³CO lines clearly demonstrate that the CO(2-1) lines are broad, with deep absorption dips caused by cold, dense gas in the light of sight. The CO and CS linewidths, indicative of the shock speed, are $20-30 \text{ km s}^{-1}$.

Both the near-infrared and millimeter-wave emission are attributed to shocks into gas with density $> 10^3$ cm⁻³. Individual shock structures are resolved in the H₂ emission, with inferred edge-on shock thickness $\sim 10^{17}$ cm, consistent with non-dissociative shocks into gas densities of 10^3 - 10^4 cm⁻³. Bright 1720 MHz OH masers are located within the shocked H₂ gas complexes and highlight

only localized areas where the conditions for masing are optimal. The H α and X-ray emission, which trace hotter shocked gas, have morphologies very different from the radio. We find a detailed correlation of the radio and H₂ emission for some long filaments, indicating cosmic ray acceleration or re-acceleration due to the shocks into moderately dense gas. Compared to the interclump gas and the very dense cores, the synchrotron emissivity of the moderate-density (CO-emitting) medium is highest, which explains the radio-H₂ correlation and the very bright radio emission of these two SNRs despite their relatively advanced age. The different morphologies of these two remnants at different wavelengths is explained by a highly nonuniform structure for giant molecular clouds, with low-density ($\sim 5~{\rm cm}^{-3}$) gas occupying most ($\sim 90\%$) of the volume, moderate density gas ($\sim 10^3~{\rm cm}^{-3}$) gas occupying most of the rest of the volume, and dense gas in cores.

This preprint is made available through astro-ph and has had its figures compressed significantly from the originals. Please see the published article (expected in Jan 2005 in the Astrophysical Journal) for higher-quality figures.

1. Introduction

W 28 and W 44 are two supernova remnants in molecular clouds. They are very bright radio sources—the 6th and 7th brightest remnants in the Green (2001) catalog—with shell-like morphologies (Dubner et al. 2000; Jones et al. 1993), located adjacent to giant molecular clouds with which they have been suspected to be interacting (Wootten 1981; Denoyer 1983). W 28 and W 44 are also paradigms of the new class of 'mixed-morphology' supernova remnants, whose shell-like, non-thermal radio emission contrasts sharply with centrally-filled, thermal X-ray emission (Long et al. 1991; Rho & Petre 1998). Both W 28 and W 44 also contain OH 1720 MHz masers attributed to dense, shocked gas (Lockett et al. 1998). Based on absorption of the radio continuum by foreground gas, the distances of W 28 and W 44 are estimated to be 1.9 kpc (Velázquez et al. 2002) and 2.5 kpc (Cox et al. 1999), respectively. Both remnants have mean radii of 11 pc. The radio shell of W 44 is non-circular, being elongated north-south and brighter on the eastern side than elsewhere. The radio shell of W 28 is much brighter and better defined on its northern side than elsewhere.

W 44 is host to the pulsar B1853+01, which is almost certainly the remnant of the progenitor star (Wolszczan, Cordes, and Dewey 1991). The presence of the pulsar yields two key clues to the nature of W 44. First, it must be the result of a core-collapse supernova from a progenitor with mass between 8 and 20 M_{\odot} : a smaller progenitor would not form

a neutron star (Woosley 1987; Wheeler 1981), while a larger one would form a black hole instead (Fryer 1999). The spectral type of the progenitor, when on the main sequence, would have been between B4 and O8. If such a star were surrounded by material with a density 1 or 10^3 cm⁻³, the H II region would have been smaller than 2 or 0.02 pc, respectively. Thus the progenitor would have had little influence on its parent molecular cloud on the size scales of the present supernova remnant (Spitzer 1978). Second, the age of the remnant is probably comparable to the spin-down age of the pulsar, 2×10^4 yr (Wolszczan, Cordes, and Dewey 1991). PSR B1853+01 also produces relativistic particles and excites a wind nebula visible in the radio (Frail et al. 1994) and X-ray (Petre et al. 2002). A relatively young pulsar, PSR B1758-23, is near W 28 but outside the remnant (Kaspi et al. 1993); the weight of current evidence suggests that this pulsar is not related to W 28 (Claussen et al. 2002). The association of W 28 with molecular clouds and its radio/X-ray morphology suggest the progenitor may also have been a core-collapse, in which case the stellar remnant is now a radio-quiet neutron star or a black hole; however, the supernova could also have been a Type I, coincidentally close to a molecular cloud.

 γ -ray sources, detected with the *Compton* Gamma Ray Observatory using EGRET, have been associated with W 28 and W 44 (Esposito et al. 1996); the updated associations using the Third EGRET source catalog (Hartman, R. C. et al. 1999) are 3EG J1800-2338 for W 28 and 3EG J1856+0114 for W 44. The angular resolution in γ -rays is insufficient (0.3°) to pinpoint their origin. The W 28 source is south of remnant center in a relatively radio-faint part of the remnant. The W 44 source is located within the remnant, with the pulsar included in its error circle. No TeV photons were detected from W 28 using CANGAROO, so the source spectrum must turn off between GeV and TeV energies (Rowell et al. 2000).

Both W 28 and W 44 have extensive evidence for interaction with molecular clouds. Early observations (Wootten 1981; Denoyer 1983) showed molecular gas near or possibly in the remnant, but the sensitivity, resolution and available millimeter-wave receivers (limited to the 3mm band) were inadequate to clearly reveal a direct interaction with the molecular clouds. X-ray observations showed that these two remnants are filled with a large amount of relatively dense ($n \sim 1 \text{ cm}^{-3}$), hot gas. The X-ray morphology contrasts markedly from the shell-like radio morphology, making W 28 and W 44 members of the "mixed-morphology" class; the existence of a significant amount of material inside the remnant was attributed to interaction of the remnant with relatively dense gas (Rho et al. 1994; Rho & Petre 1998).

The most clear-cut evidence for interaction between the supernova remnants and molecular clouds is the detection of emission from the shocked molecules themselves. The molecules can be directly detected in four ways: millimeter-wave emission lines with linewidths much greater than those of cold gas, OH 1720 MHz maser emission, far-infrared line emission, and

near-infrared H₂ emission. (1) Broad molecular line emission has clearly been detected from W 44 using $CO(1 \rightarrow 0)$ and $CO(2 \rightarrow 1)$ observations (Seta et al. 1998), and from W 28 using a small telescope to map the remnant in the $CO(3 \rightarrow 2)$ line (Arikawa et al. 1999). The linewidths $\sim 20-30~\rm km~s^{-1}$ FWHM, with maximum extents up to 70 km s⁻¹ in some locations, clearly distinguish the shocked gas from the cold, ambient gas. (2) OH 1720 MHz maser emission has been detected from W 28 (Frail et al. 1994a) and observed in more detail for both W 28 and W 44 (Claussen et al. 1997) using the NRAO Very Large Array. These 1720 MHz OH masers have been interpreted as spots of amplified radio emission through clumps of OH gas with densities and temperatures characteristic of modest-density ($n \sim 10^3$ cm⁻³) gas that has been shocked by modest-velocity ($v \sim 20 \text{ km s}^{-1}$) non-dissociative shocks (Lockett et al. 1998; Wardle and Yusef-Zadeh 2002). The brightest maser emission arises from small spots with high amplification. VLBI observations yield upper limits to the angular sizes from 0.05–0.18", with very strong measured magnetic field strengths of 2 mG (Claussen et al. 1999). Recent radio spectral observations of W 28 showed that the normal, thermal absorption in the main OH lines can trace the shocked gas, because the absorption lines have broad line widths; faint satellite line emission (probably weak masers), has a narrow line width and covers much more area than just the maser peaks (Yusef-Zadeh et al. 2003). There now appears to be a strong association between 'mixed morphology' supernova remnants and maser-emitting supernova remnants (Yusef-Zadeh et al. 2003), suggesting that while W 28, W 44, and IC 443 may be prototypes of molecular-cloud-interacting supernova remnants, the total number could be much higher. (3) Highly-excited far-infrared $CO(16 \rightarrow 15)$ and mid-infrared H₂ (S3 and S9) emission, together with all of the atomic fine structure lines expected from shocks into moderate-density gas, were detected from W 28 and W 44 using the *Infrared Space Observatory* (Reach & Rho 1998, 2000). (4) Near-infrared H₂ emission is predicted to be one of the main coolants of shocks in dense gas (Draine et al. 1983). Bright H_2 2.12 μ m emission has been detected from IC 443 (Burton et al. 1988; Rho et al. 2001), and 3C 391 (Reach et al. 2002). Near-infrared emission from W 28 and W 44 has not yet been reported, and one of the main goals of this paper is to present our new observations and their implications.

Some relevant theoretical models have recently been published. A model was developed specifically for W 44, attempting to explain its observed features across an exceptionally wide range of observed properties, analytically by Cox et al. (1999) and numerically by Shelton et al. (1999). They explain many properties of the remnant as the result of a shock propagating into an essentially uniform medium with a density of $n_0 = 6$ cm⁻³. The hot interior of the remnant is relatively dense in their model, $n_{int} = 1$ cm⁻³, as required to explain the centrally-filled X-rays. This model does not include denser gas. Chevalier (1999) published a model of a supernova remnant in a molecular cloud. This model is generally similar to that of Cox

et al. (1999), because most of the observable properties are due to shocks in the interclump gas with a pre-shock density $n_0 = 4-5$ cm⁻³; however, Chevalier (1999) also discussed some of the consequences of denser material. Based on these models, one would infer that some giant molecular clouds are predominantly composed of material of much lower density than is capable of producing the features that define giant molecular clouds, such as CO emission, gravitational binding, and star formation. Low-density $(n < 10 \text{ cm}^{-3})$ material is either diffuse (tenuous, transient, and unbound) or is present together with other material that we know of as the molecular cloud and dominates the mass and most other observable properties. How can these two different views of molecular clouds be reconciled?

The observations of W 28 and W 44 provide a special opportunity to determine the structure of giant molecular clouds by studying the results of 10⁵¹ erg explosions inside the clouds. By observing the results of a supernova explosion in the cloud, we can determine whether (1) the shock expands unimpeded, as would occur if the filling factor of dense gas is very small and there is no interclump gas; or (2) the shocks propagate primarily in the dense gas, as would occur if its filling factor is large; or (3) the shock is not significantly affected by the dense gas (having low filling factor) but propagates primarily into low-density, interclump gas. A wide range of supernova remnant morphologies is possible, and at least three pre-shock density regimes have been inferred from the range of gas coolants in far-infrared spectra (Reach & Rho 2000). By observing the shocked molecular gas directly, and at unprecedented sensitivity and resolution, we can better explain the current remnant morphology and begin to attribute different aspects of the supernova remnants to specific properties of the parent molecular clouds.

After this Introduction, we summarize the new observations that we performed: widearea millimeter wave CO observations, high-resolution millimeter-wave CO and CS observations, and near-infrared H₂ observations. Then we describe the results for each remnant in detail. With all of the observations and results in hand, we then compare the shocks as traced by near-infrared and millimeter-wave emission and attempt to separate pre-shock gas, gas experiencing dissociative shocks, and gas experiencing non-dissociative shocks. We discuss the implications of our observations for the origin of synchrotron radiation from mature supernova remnants and for cosmic ray acceleration. Finally, we explain why the properties of the ambient medium that we infer from infrared and millimeter observation of shocked clumps and filaments is so different from the properties inferred from X-ray and radio observations of the supernova shell and hot interior.

2. Observations

2.1. CO Survey data

The parent clouds with which the remnants are interacting, and from which the progenitors presumably formed, can be seen in CO surveys of the galactic plane. Previous studies of these remnants have referred to a wide range of structures in the interstellar medium as being associated with the remnants, including H I emission and absorption (Knapp and Kerr 1974; Denoyer 1983; Velázquez et al. 2002) and limited CO mapping (Dickel, Dickel, and Crutcher 1976; Wootten 1977, 1981; Seta et al. 1998) which trace parts of the clouds but don't reveal their full extents.

Figure 1 shows the CO images of the parent molecular clouds. The CO data are from the reprocessed survey Dame, Hartmann, and Thaddeus (2001), including the inner galaxy data originally from Bitran et al. (1997). W 44 is located in a well-defined, giant molecular cloud that is clearly distinguished from surrounding material; the cloud is centered at $l = 35.0^{\circ}$, $b = -0.7^{\circ}$, v = 44 km s⁻¹, with a radius of 58 pc and a total mass of 1.8×10^{6} M_{\odot} (Dame et al. 1986). The parent cloud for W 28 can be discerned in the CO data-cube for the inner galaxy (Dame, Hartmann, and Thaddeus 2001); it is centered at $l = 6.6^{\circ}$, $b = 0.0^{\circ}$, v = 19 km s⁻¹, with a diameter ~ 25 pc and a mass of 1.4×10^{6} M_{\odot} . The similar radio and X-ray morphologies, ages, locations near molecular clouds, and parent molecular cloud properties make W 44 and W 28 a good pair of remnants to study together.

Fig. 1.— FIGURE NOT INCLUDED IN TEX FILE. SEE FILE fla.jpg and flb.jpg. CO images of the giant molecular clouds containing the supernova remnants W 44 and W 28. Contours are at constant CO(1-0) antenna temperature, ranging from 1–30 K (0.65 km s⁻¹ channel) and 3–12 K (1.3 km s⁻¹ channel) for W 44 and W 28, respectively. The thick circle with dashed cross-hairs through the center indicates the size and center of the radio emission from each remnant. A smaller circle, to the left of the W 28, indicates the location of the Trifid Nebula.

2.2. NRAO/Steward Observatory 12-meter Observations

Observations were performed in March 1997 and November 2002 with the 12-m millimeter-wave telescope on Kitt Peak. The observations were made using the On-The-Fly technique, whereby the telescope was slewed in right ascension at a constant rate of 30 and 10 "/s, and spectra were taken at 0.1 sec intervals, which finely samples the telescope beam of 53" and 26" at 115 and 230 GHz, respectively. In March 1997, the eastern half of W 44 was

mapped in the $CO(1 \to 0)$ line (115 GHz), and regions surrounding some of the apparent shock interactions in W 44 and W 28 were mapped in the $CO(2 \to 1)$ line (230 GHz). In November 2002, a complete map of W 44 was made in the $CO(2 \to 1)$ line.

The $CO(1 \to 0)$ observations of W 44 reveal extensive emission covering the entire region. On large scales, the dominant feature is the giant molecular cloud (GMC) at a velocity of 43 km/s with lines that are typically 10 km s⁻¹ wide (with substructure); this is consistent with the overall giant molecular cloud described above. There were no clear indications of shock-broadened molecular lines from the $CO(1 \to 0)$ observations; most of the broadening is due to the same combination of gravity, turbulence, and magnetic pressure that generates the linewidths observed from this and other GMCs.

The $CO(2 \to 1)$ observations of both W 28 and W 44 also reveal extensive emission, with a great deal of structure both spatially and spectrally. The separation of the emission into parent cloud, shocked gas, and foreground absorption requires understanding the 'geography' of each remnant, which we describe in § 3 and 4 for W 44 and W 28, respectively.

2.3. IRAM 30-meter Observations

On September 16-22, 1997, we observed W 44 and W 28 using the IRAM 30-m telescope on Pico Veleta, Spain. Some spectra were also obtained from our earlier November 22-29, 1996 observing run. These observations cover small portions of the remnants, selected based on the 12-m maps and the $CO(1 \rightarrow 0)$ maps of Seta et al. (1998). The observing procedure, calibration, and data reduction for these observations were the same as described for our previous observations (Reach & Rho 1999). Three receivers were used to simultaneously observe three different spectral lines at 1.3, 2, and 3 mm. The weather during the 1997 observing run included freezing rain, but had usable periods of haze. The receivers were tuned to the $CS(2 \rightarrow 1)$, $CS(3 \rightarrow 2)$, and $CO(2 \rightarrow 1)$ lines, with system temperatures typically 330, 520, and 1300 K. Very few lines of sight produced detectable $CS(2 \rightarrow 1)$ so we tuned the 3 mm receiver to $SiO(2 \rightarrow 1, v=0)$ for the last half of the run. The weather during the 1996 run was better, which allowed $CS(3 \rightarrow 2)$ and $CS(5 \rightarrow 4)$ observations.

2.4. Palomar Observations

On July 12-13, 2001, and August 16-17, 2002, we observed portions of the W 44 and W 28 (and other supernova remnants) using the Prime Focus Infrared Camera (PFIRCAM) on the Hale 200-inch telescope on Mount Palomar. The PFIRCAM has a 256×256 pixel

array, with a pixel scale of 0.494" at the f/3.3 prime focus of the 200-inch telescope. In 2001, the weather was hazy, with 1.5" seeing. In 2002, the weather was very good, with 0.8" seeing on both nights. Two fields (the western portion of W 44, and the eastern portion of W 28) were re-observed using the new Wide-Field Infrared Camera (WIRC), a 2048×2048 camera with 0.25" pixels, on August 9, 2003, also under very good conditions (0.9"). Our observing strategy, calibration, and data reduction were the same as for our previous observations (Reach et al. 2002). In summary, we made dithered rasters switching between the remnant and a reference position outside the remnant, combined the reference observations to make a sky image, and combined sky-subtracted images on the remnant into mosaics. The data reduction procedure was improved to take full advantage of 2MASS (Skrutskie 1999) astrometry, by locating cataloged stars on each image, determining an accurate world coordinate system for each image, then generating the combined mosaic. The calibration procedure was refined to use improved 2MASS magnitudes from recent reprocessing, and we restricted the range of magnitudes for calibrators to be well within the range of high-confidence detection 2MASS and linearity in PFIRCAM.

All regions were observed through the $\rm H_2$ 2.12 $\mu \rm m$ filter, which is 1% wide in PFIRCAM and 1.5% in WIRC. Smaller regions were observed in other narrow (1% wide) filters to measure the continuum at 2.2 $\mu \rm m$, the [fe II] 1.64 $\mu \rm m$ line and nearby continuum, and the Paschen β 1.28 $\mu \rm m$ line. Extended emission was present in both the $\rm H_2$ and [fe II] filters for W 44 and W 28. No extended emission was detected in the continuum filters or $\rm P\beta$ (< $\rm 10^{-5}$ erg s⁻¹ cm⁻² sr⁻¹). Therefore, continuum subtraction is neither needed nor performed on the observations presented below. Some artifacts remain in the PFIRCAM images, specifically: faint ghost images located 13" NW (position angle -61°) from very bright sources (nearly impossible to discern in the published images because of the huge number of real stars that are brighter than the ghost images); and rays of stray light when stars fall on the edge of the detector (some were masked by hand and appear as polygonal cutouts). The observations have a noise level of $\rm 0.5-1 \times 10^{-5}$ erg s⁻¹ cm⁻² sr⁻¹ per pixel. The absolute calibration is accurate to better than 20%, and the narrow-band directly measure the surface brightness of the shocked gas except in positions containing stars.

2.5. Other observational data

To complement the new CO and molecular data, we requested radio and optical images from other researchers. Supernova remnants are most clearly traced by nonthermal radio continuum emission, so the best maps of overall remnant geography are low-frequency but high-resolution radio images. For W 44, we used the VLA image of Jones et al. (1993) at

a frequency of 1465 MHz; the 15" angular resolution and low (1.5 mJy/beam) noise of this image clearly reveals the filamentary internal structure of the remnant. The astrometry was corrected by comparing to the high-resolution radio image of the W 44 pulsar wind nebula published by Frail et al. (1994), using the pulsar as a guide point. For W 28, we used the VLA image of Dubner et al. (2000) at a frequency of 328 MHz; the $92'' \times 52''$ angular resolution is not good but the remnant is cleanly separated from thermal emission. We compared this image to the portion of the Frail et al. (1994b) image that covered W 28 serendipitously and very found good correspondence of the remnant features, as expected.

 ${\rm H}\alpha$ images of W 28 and W 44 were created by combining digitized, deep (3 hr) plates taken at the 48-inch UK Schmidt telescope and provided as part of the SuperCOSMOS ${\rm H}\alpha$ Survey (Parker & Phillipps 1998; Malin 1998; MacGillivray 1998). The line filter has a 1% width centered on 6590 Å. Images through the narrow continuum filter show no extended emission, so we did not subtract them from the ${\rm H}\alpha$ images used here. To verify the astrometry, we compared the reprojected, combined ${\rm H}\alpha$ mosaic to the Digitized Sky Survey and HD catalog stars; the DSS and HD positions were within 1" while there was an offset of 9" in the ${\rm H}\alpha$ image, which we corrected. The ${\rm H}\alpha$ emission from W 28 has been described before by Van den Bergh, Marscher, & Terzian (1973), but the new image is much deeper and has been digitized, enabling a detailed comparison with the radio and other images.

3. Results for W 44

To get oriented within W 44, Figure 2 shows the radio image together with outlines of the observed regions. The radio emission arises from a limb-brightened shell that breaks into prominent filaments, many of which appear to emanate from the southeast. The radio emission is generally much brighter on the eastern hemisphere, but there is a knot of bright radio emission on the westernmost portion of the shell as well.

Fig. 2.— FIGURE NOT INCLUDED IN TEX FILE. SEE FILE f2.jpg. Finder chart for W 44 showing the locations of the three Palomar images of H₂ emission (Map1, Map2, and Map5) as solid rectangles, the OH masers from Claussen et al. (1997) and 'Prominent Wing' (PW) and 'Wing Candidate' (WC) positions from Seta (1995) as asterisks. The locations of mm-wave CO observations are shown as dashed rectangles. The smaller, dotted boxes within Map1 and Map2 (and all of Map5) were observed in the Fe II filter. These symbols and rectangles are superposed on the radio image from Jones et al. (1993) and a J2000 coordinate grid.

3.1. Millimeter-wave results for W 44

The $CO(2 \to 1)$ osbervations with the 12-m telescope covered the entire remnant (with low sensitivity). Figure 3 shows intensity maps in different velocity ranges. Each velocity range corresponds (in central velocity and width) to one of the several spectral components that are present in this field. The giant molecular cloud associated with W 44 appears in Figures 3e-f. The cloud clearly extends past the edges of our image, in particular to the north and east, consistent with the giant molecular cloud in Figure 1. The spectrum averaged over the portion of the giant molecular cloud in our image reveals a simple, Gaussian line profile centered at 46.6 km s⁻¹, with a linewidth of 4.1 ± 0.2 km s⁻¹, a peak brightness temperature of 6.9 K, and a line integral W[CO(2 \rightarrow 1)] of 30 K km s⁻¹. Using $N(\rm H_2)/W$ [$CO(1 \rightarrow 0)$] = 3×10^{20} cm⁻² K⁻¹ km⁻¹s (Bloemen et al. 1986), this cloud has a column density $N(H_2) = 1.1 \times 10^{22}$ cm⁻². The column density inferred from absorption of X-rays from the interior of the remnant is $N(H) = 2 \times 10^{22} \text{ cm}^{-2}$ (Rho et al. 1994); assuming most of the gas is molecular, this would correspond to $N(H_2) = 1 \times 10^{22} \text{ cm}^{-2}$ and agrees well with the column density inferred from the CO observations, suggesting that much of the parent cloud is in front of the remnant. The velocity of this cloud is consistent with galactic rotation at the longitude and distance of W 44. This is the ambient molecular cloud with which W 44 is interacting and from which the progenitor star probably formed.

The northeastern ridge of bright radio emission is closely parallel to the surface of the molecular cloud as traced in Figure 3e. It appears that the W 44 progenitor exploded within, and just to the west of the center of, its parent molecular cloud. There is ambient gas from the parent all around the remnant. Figure 3f shows a piece of the west of the remnant; the interaction of the remnant with this gas probably explains the very bright, western radio knot, for which we present new observations of shocked gas below. The presence of ambient molecular gas all around W 44 makes it a special case of a supernova within a molecular cloud. A similar situation was found in 3C 391, though its progenitor was relatively closer to the edge of its parent molecular cloud or even just outside (Wilner, Reynolds, & Moffett 1998). Before the supernova, the progenitor of W 44 would have generated only a very small H II region, even if it had been an O star, because the surrounding medium is relatively dense.

In addition to the ambient cloud, the CO observations reveal several other features that can be distinguished in the maps at velocities different from the ambient cloud. Figure 3a shows two very distinct clouds at 95 km s⁻¹. The spectra of these clouds shows they have very narrow linewidths, comparable to our resolution. The lines appear in both $CO(1 \rightarrow 0)$ and $CO(2 \rightarrow 1)$. The northeastern 95 km s⁻¹ clump is located within the radio contours of the remnant, while the southern one is just south of the remnant. Using the rotation

Fig. 3.— FIGURE NOT INCLUDED IN TEX FILE. SEE FILE f3.jpg. Images of W44 in the $CO(2 \rightarrow 1)$ line. Each panel shows the integrated emission over a different velocity range, corresponding to each major component of the CO line in the surveyed region: (a) 94.9–97.5 km s⁻¹, (b) 80.6–88.4 km s⁻¹, (c) 72.8–79.3 km s⁻¹, (d) 54.6–59.8 km s⁻¹, (e) 45.4–52.0 km s⁻¹, (f) 38.9–42.8 km s⁻¹, (g) 29.8–37.6 km s⁻¹, (h) 15.5–25.9 km s⁻¹. Panel (i) is the radio image, in the exact same projection and scale.

curve of Burton (1988), the highest allowed velocity at this galactic longitude is 95 km s⁻¹, meaning they would have to be near the tangent point (5–7 kpc) if their velocity were only due to galactic rotation. The narrow $CO(1 \rightarrow 0)$ linewidths (< 1.5 km s⁻¹) indicate that the clumps are cold, and probably not from shocked gas. It is possible that these clouds are interacting with the remnant, but based on the available evidence, we suspect that they are background clouds unrelated to W 44.

Molecular gas currently undergoing shocks should have a linewidth greater than that of the parent molecular cloud. Such broad molecular line regions appear bright in at least 4 panels of Figure 3g shows emission at velocities less positive than the ambient gas, due to gas that is approaching the Sun faster than the ambient cloud. Three features can be seen in this image: a set of peaks near and just inside the eastern radio rim, a peak in the south-central part of the remnant, and a large faint region inside the western part of the remnant. The latter region appears only in panel g and is apparently a narrow CO line, due to cold gas and not necessarily associated with the remnant. The northeastern and southern regions, however, appear in multiple panels. The spectra of these regions show broad molecular lines extending mostly toward lower velocities, meaning the shocks are moving toward us. The line of sight from the Sun therefore passes through the ambient gas, the shock front, the cooling gas, and then the remnant interior. The high X-ray absorption, consistent with the total parent cloud column density, supports the idea that the bulk of the ambient molecular gas is located in between the remnant and the Sun. It appears the progenitor exploded on the far side and just west of a dense portion of the parent cloud.

The IRAM 30-m observations reveal the shocked gas at higher angular resolution and sensitivity. The regions observed with the IRAM 30-m were selected using the radio image, OH 1720 MHz maser positions (Claussen et al. 1997), and Nobeyama 45-m observations (Seta et al. 2004) as a guide. Table 1 shows the coordinates around which small maps were made and the locations of some other points of interest within these maps.

Figure 4 shows the spectra obtained toward 6 OH maser locations within W 44. Toward all positions, there is a broad molecular line. The $CS(5 \rightarrow 4)$ emission is only detected from a limited number of positions, and the $CS(3 \rightarrow 2)$ spectra are mostly too noisy to be

useful. The broad emission lines are mixed with narrower components, sometimes at the same velocity and sometimes shifted. The presence of the broad emission line confirms that at least part of the emission from W 44 is due to shocked gas. Earlier observations by Seta et al. (1998) also showed broad emission lines in $CO(1 \rightarrow 0)$, and we confirm that the positions they identified as having prominent wings do indeed have broad $CO(2 \to 1)$ lines. Using the higher rotational transition has some advantages, making our data somewhat cleaner than the earlier observations. Specifically, the upper energy level is relatively more excited in the shocked gas than in the unshocked gas, increasing the brightness of the shocked gas relative to the unshocked gas. Further, the line-of-sight absorption is stronger for the 1-0 transition, which can be absorbed by cold gas with substantial populations in the ground state, than for the 2-1 transition. Neither of these effects are dramatic improvements, because the J=2level can be excited by the unshocked gas (leading to narrow emission lines from the cold gas along the line of sight) and the J=1 level has a substantial population in the unshocked gas (leading to narrow absorption lines from the cold gas along the line of sight). However, the combined effects, together with the higher angular resolution at the higher observing frequency, make these new data significantly cleaner in tracing the shocked gas.

Fig. 4.— FIGURE NOT INCLUDED IN TEX FILE. SEE FILE f4.jpg. Spectra of $CO(2 \to 1)$, $CS(2 \to 1)$, and $^{13}CO(1 \to 0)$ lines toward 8 positions in W 44, with their locations indicated on the superposed radio continuum image (as in Fig. 2). Panel (a) shows the spectrum of the ambient gas outside the remnant. In the other panels, the thick spectrum with a baseline at 0 K is $CO(2 \to 1)$, the thin spectrum with a baseline at -4 K is the $CS(2 \to 1)$ line (with intensity multiplied by 10), and the thin line with a baseline at +21 K is the $^{13}CO(1 \to 0)$ line (with intensity multiplied by -3).

To investigate the distribution of the shocked gas relative to the unshocked gas, we made small maps around a few positions that showed broad emission lines. Figure 5 shows the $CO(2 \rightarrow 1)$ spectrum for a position near W 44:OHE with a clear, broad component and a superposed narrow emission component. The full-width-at-half-maximum (FWHM) of the narrow component is 5.2 km s⁻¹, typical of the ambient molecular cloud around W 44. The FWHM of the broad component is 30.5 km s⁻¹, which is far wider than ambient gas and is due to shocks with speeds equal to or greater than (due to projection) 30.5 km s⁻¹ into dense gas. The amplitude of the broad component near W 44:OHE varies significantly from position to position, while the narrow component is widespread. The location where the broad component is brightest is not coincident with an OH maser. A similar result was found in the broad molecular line region in 3C 391, where an OH maser located between the peaks of the broad and narrow components (Reach et al. 2002).

Another position of interest is W 44:PW1, the location of a 'prominent wing,' also called

Fig. 5.— FIGURE NOT INCLUDED IN TEX FILE. SEE FILE f5.jpg. $CO(2 \rightarrow 1)$ and $^{13}CO(1 \rightarrow 0)$ spectra toward W 44:OHE. The narrow component in the $CO(2 \rightarrow 1)$ spectrum aligns exactly with the peak in the $^{13}CO(1 \rightarrow 0)$ spectrum, suggesting that the cold gas does not absorb the emission from the shocked gas (which makes the wide component); the cold gas is probably behind the shocked gas.

'Wing 1,' which was found from Nobeyama 45-m $CO(1 \rightarrow 0)$ observations (Seta 1995; Seta et al. 2004). Figure 4(h) shows the $CO(2 \rightarrow 1)$ spectrum and the $^{13}CO(1-0)$ spectrum toward this position. The $CO(2 \rightarrow 1)$ emission is clearly broad, but with a double-humped structure that could be mistaken for multiple, moderately-broad components along the line of sight. The double-humped structure is actually due to a deep absorption trough cut into a single broad emission component. The ¹³CO(1-0) emission, which traces the total column density and is dominated by the cold gas along the line of sight, matches very well the center and width of the apparent 'notch' cut out of the $CO(2 \to 1)$ spectrum. The optical depth of the absorbing CO in the J=1 level is $\tau > 1$ to produce this trough. Such an optical depth is consistent with the column density of the parent molecular cloud (and its location in front of the remnant) as discussed above. Inspecting the spectra near W 44:PW1, the narrow absorption component transforms into a narrow emission component in locations where there is no broad molecular line emission. This can be explained by a combination of geometry and physical conditions. When there is bright emission from hot, shocked gas behind cold, unshocked gas, an absorption component appears. Then, when the column density of shocked gas is small enough that its brightness temperature is lower than that of the shocked gas, or the cold gas is behind the hot gas, the narrow component appears in emission.

The depth, velocity, and location of the molecular absorption features suggests they are due to pre-shock gas. Figure 6 shows high-quality spectra of $CO(2 \to 1)$, $HCO^+(1 \to 0)$, and $^{13}CO(1 \to 0)$. The HCO^+ spectra are similar to the $CO(2 \to 1)$ spectra, with deep absorption near the line center and even broader wings. The HCO^+ line is even more susceptible to absorption than $CO(2 \to 1)$ because it is a ground-state transition with a larger dipole moment. The optical depth in the core of the $HCO^+(1 \to 0)$ line is ~ 2 , with a width ~ 10 km s⁻¹ consisting of multiple components. The required column density of HCO^+ in the ground state is $N[HCO^+] = 1.03 \times 10^{12} \tau \Delta v$ cm⁻² which amounts to 2×10^{13} cm⁻². If the abundance of HCO^+ relative to H_2 is 2×10^{-9} typical of molecular clouds (Liszt and Lucas 2000), then the inferred column density in the absorbing cloud is $N[H_2] \sim 1 \times 10^{22}$ cm⁻². This column density agrees very well with that of the parent molecular cloud, based on the $CO(1 \to 0)$ brightness and X-ray absorption. Because it is at the same velocity and spatial location as the remnant, they must be close together, with the absorbing gas being

the unshocked portion of the parent molecular cloud along the line of sight.

Fig. 6.— FIGURE NOT INCLUDED IN TEX FILE. SEE FILE f6.jpg. 12 CO(2-1), HCO⁺(1-0), and 13 CO(1-0) spectra toward three positions in W 44. In each panel, the lower spectrum is HCO⁺(1-0), multiplied by a factor of three and shifted downward by 5 K; the middle spectrum is 12 CO(2-1); and the upper spectrum is 13 CO(1-0), inverted and multiplied by a factor of two and shifted upward by 20 K. In panels (a) and (b), the deep troughs in the 12 CO(2-1) and HCO⁺(1-0) spectra near the parent cloud velocity (indicated by the dashed line) align with the peaks in 13 CO(1-0) spectrum, suggesting that cold gas in front of the shocked region absorbs the hot, shocked gas.

The CO emission in the southern portion of W 44 was observed in some detail. It appears as a broad-line region in the NRAO 12-m observations: in Figure 3e it appears as a roughly north-south filament starting just inside the southernmost boundary of the remnant. The region contains the maser complexes W 44:OHB and W 44:OHC. The area mapped with the IRAM 30-m is indicated in Figure 2 as a dashed box labeled 'CO [30-m]'. Figure 7 shows the grid of spectra, which vary dramatically from position to position. A broad emission line is clearly evident in a region extending from offsets (0,0) to (80,-260). In the spectra at the top of Figure 7, the emission arises from a set of narrow components. It is possible that this is actually broad-line emission being absorbed by foreground gas, as was found for W 44:PW1, W 44:PW3, and W 44:OHF; but we only have the 13 CO or HCO+ observations that disentangle the absorption and emission for a few lines of sight in the remnant. The angular resolution of the 30-m telescope in the CO(2 \rightarrow 1) line is about 10.5", much smaller than the region over which broad emission lines are observed, so it is clear that the emitting regions are extended. The profiles tend to have a wider wing on the low-velocity side, suggesting that the gas is being accelerated toward us.

3.2. Near-infrared results for W 44

Turning to the near-infrared observations, the 2.12 μ m H₂ images are striking in appearance, with an intricate network of filaments and some isolated bright clumps. The three regions that were observed in the near-infrared also contain regions with bright O I 63 μ m emission (Reach & Rho 1996), OH masers (Claussen et al. 1997), and broad molecular lines (Seta et al. 2004). In the W 44 northeastern image (Fig. 8), a ridge of H₂ emission follows the edge of the radio supernova remnant, which runs diagonally across the upper left portion of the image. The H₂ emission contains bright filaments and arcs as well as a more diffuse component that generally envelops the brighter features. Some of the filaments are

Fig. 7.— FIGURE NOT INCLUDED IN TEX FILE. SEE FILE f7.jpg. Grid of spectra near W 44:OHB. The grid is labeled with the offsets (in arcsec) East and North of the nominal position W 44:OHB. There are both wide and narrow components throughout this region. The bottom of the figure covers the edge of the remnant, and the bottom right is somewhat outside the remnant, giving an idea of the baseline, random emission around the remnant. Around (0'',80''), the emission appears to be two medium-wide components, but this is probably due to absorption by cold gas in front of the remnant. The range of appearances of these spectra is due to a complicated mix of emission and absorption with different angular distributions and velocity widths. There are two OH masers in this region, at (0,0) and (37,-243).

extremely narrow and probably represent individual shock fronts seen close to edge on; these are discussed in §5.4 below. The other structures, and the diffuse emission, are probably an amalgam of multiple shock fronts seen from a range of angles. Significant shocked H₂ emission is detected interior to the radio shell, for example in the lower-central portion of the image.

The W 44 southern image (Fig. 9 greyscale, Fig. 10 color) is the most detailed, having 4 times as much integration per pixel as the other H₂ images. Two bright sets of filaments run diagonally across the field, with fainter filaments (all in the same general direction) distributed throughout the field. A very bright knot of H₂ emission lies just below the upper filament in Fig. 9. This is not a star or an artifact; it is just burned out in the greyscale image. There are some narrow filaments that appear to be individual edge-on shock fronts, but for the most part the bright filaments have significant substructure indicating they comprise multiple shock fronts.

The W 44 western field (Fig. 11) contains some very bright filaments, again roughly parallel to the edge of the remnant, which runs roughly north-south at this location. It is possible to see individual shock fronts in this image; counting across the image along a single line (from the upper left to the lower right), there are at least 15 individual shock fronts. This shows clearly that the pre-shock medium was highly structured with gaps between regions containing the gas with density appropriate to generate bright H₂ after being shocked.

Fig. 8.— FIGURE NOT INCLUDED IN TEX FILE. SEE FILE f8.jpg. H_2 2.12 μ m image of the northeastern portion of W 44 (Map1). The portion of the supernova remnant covered by this image is indicated in Fig. 2. The greyscale ranges from 0 (white) to 1×10^{-4} erg s⁻¹ cm⁻² sr⁻¹ (black) in this and the other near-infrared images in this paper.

Table 1: Positions for Maps made at IRAM 30-m^a

Position	RA (2000)	Dec	Δ RA	Δ Dec	Description
W 44:OHE	18 56 28.1	+01 29 59	0	0	OH maser (Claussen et al. 1997)
OHF	$18\ 56\ 36.7$	$+01\ 26\ 32$	129	-207	OH maser (Claussen et al. 1997)
PW1	$18\ 56\ 12.7$	$+01\ 26\ 25$	-230	-214	Prominent CO(1-0) wing (Seta 1995); 'Wing 1'
PW3	$18\ 56\ 11.7$	$+01\ 27\ 55$	-246	124	"
W 44:OHA	$18\ 52\ 55.2$	$+01\ 29\ 51$	0	0	OH maser (Claussen et al. 1997)
W 44:OHB	$18\ 56\ 01.2$	$+01\ 12\ 47$	0	0	"
OHC	$18\ 56\ 03.7$	$+01\ 08\ 44$	37	-243	"
W 44:OHD	$18\ 56\ 29.4$	$+01\ 20\ 26$	0	0	"

^a Reference position: offset (412", -3621") from W 44:OHE

Fig. 9.— FIGURE NOT INCLUDED IN TEX FILE. SEE FILE f9.jpg. H_2 2.12 μ m image of the southern portion of W 44 (Map2). The portion of the supernova remnant covered by this image is indicated in Fig. 2. The clump of exceptionally bright H_2 emission discussed in the text is indicated by a black rectangle.

Fig. 10.— Color version of the H_2 2.12 μm image of the southern portion of W 44 (Map2). FIGURE NOT INCLUDED IN ASTRO-PH SUBMISSION. SEE ApJ ARTICLE

Fig. 11.— FIGURE NOT INCLUDED IN TEX FILE. SEE FILE f11.jpg. H_2 2.12 μ m image of the western portion of W 44 (Map5).

4. Results for W 28

An orientation chart showing the regions observed toward W 28 is shown in Figure 12. The main geographical features of W 28 are a semi-circular radio shell that is brightest in the north and east, and a bar (or inner shell) that extends east-west. The observed regions include most of the OH masers (Claussen et al. 1997), the bright radio ridges, and the $CO(3 \rightarrow 2)$ ridge (Arikawa et al. 1999).

4.1. Millimeter-wave results for W 28

The 12-m CO observations covered a $9' \times 13'$ region centered on the bright eastern radio ridge, containing many OH 1720 MHz masers (Frail et al. 1994a). Figure 13 shows a set of velocity-integrated images. Broad molecular line (BML) regions are those that appear in multiple images, in particular those away from the line core. Five broad-molecular-line regions can be identified in these images; Table 2 lists their positions and gaussian fits to the line profiles. The BML regions are even more easily seen in the position-velocity images; Figure 14 shows position-velocity slices through the spectral data. The exceptionally wide velocity dispersion of the BML regions compared to the ambient gas (which has typical width less than 7 km s⁻¹ FWHM) is evident. It is also evident that the BML regions are well-defined peaks. There is more extensive, broad-line-emitting gas, but the BML regions in Figures 13 and 14 are clumps (probably containing significant structure unresolved in our 30'' beam). A position-velocity slice through the northern radio shell in $CO(3 \rightarrow 2)$ was shown by Arikawa et al. (1999) [their Fig. 2], and the $CO(3 \rightarrow 2)$ image [their Fig. 3] shows extended BML emission, so the peaks listed in our Table 2 are only a subset of the BML regions in W 28.

The IRAM 30-m observations of W 28 reveal the bright CO emission at higher angular resolution. Figure 15 shows a grid of spectra centered on some of the brightest CO emission, including the broad-line positions BML3 and BML4. The broad-line emission is widespread, and it is deeply cut by narrow absorption at approximately the same central velocity (8 km s⁻¹). The absorption is particularly deep toward W 28:BML4, with an optical depth

Fig. 12.— FIGURE NOT INCLUDED IN TEX FILE. SEE FILE f12.jpg. Finder chart for W 28 showing the locations of the Palomar images of H₂ emission as a solid polygon, and the locations of CO observations with the 12-m as a dashed polygon, the OH masers from Claussen et al. (1997) as asterisks, and the BML positions as diamonds, superposed on the radio image from Dubner et al. (2000).

Fig. 13.— FIGURE NOT INCLUDED IN TEX FILE. SEE FILE f13.jpg. $CO(2 \rightarrow 1)$ maps of the eastern ridge of W 28 integrated over 9 different velocity ranges: (a) 48.28 to 63.88, (b) 40.48 to 46.98, (c) 28.77 to 37.88, (d) 15.12 to 28.12, (e) 4.074 to 7.975, (f) -4.376 to 2.124, (g) -17.37 to -5.027, (h) -33.63 to -18.02, (i) -53.13 to -34.28 km s⁻¹. Each of these velocity ranges corresponds to a peak in a spectrum, somewhere within the mapped region. The locations of 5 broad-molecular-line (BML) regions are indicated by asterisks and are labeled in panel (a). Contours are at integer multiples of 14 K km s⁻¹.

Fig. 14.— FIGURE NOT INCLUDED IN TEX FILE. SEE FILE f14.jpg. $CO(2 \rightarrow 1)$ position-velocity maps: (a) cut at constant RA $18^h01^m52^s$; (b) cut at Dec $-23^\circ25'15''$. The locations of two broad-molecular line regions that are intersected by the cuts are indicated. Contours are at integer multiples of 2 K. The positions are labeled in decimal degrees, both for declination (a) and right ascension(b).

> 1 and width ~ 1 km s⁻¹ FWHM. The absorption is patchy, but cold gas at this velocity is present throughout the region; emission lines from the cold gas are seen in the spectra with weaker broad-line emission. Three OH masers are included within the boundaries of this map; there is nothing noticeably special about the spectra centered on the OH masers.

Figure 16 shows the spectra of 4 of the 5 broad-molecular-line (BML) regions from Table 2 in the $CO(2 \to 1)$, $CS(2 \to 1)$, and $CS(3 \to 2)$ lines. The $CO(2 \to 1)$ lines are characterized by a moderately broad (20–30 km s-1) component with narrow absorptions biting notches out of the broad line profile for W 28:BML2 and BML4. Table 2 shows the brightnesses and velocities of the various lines, determined using gaussian fits. For BML2 and BML4, the $CO(2 \to 1)$ absorption notches are listed separately as negative gaussians. For BML3, the line profiles were best fit with a sum of broad and narrow gaussian; this does not mean that there are two separate components, as the combination of foreground absorption and non-gaussian profile can give the impression of two components even when there is only a single emission component. Recall that both W 28 and W 44 are located far from the Sun and near the galactic plane, so there are several clouds between the remnants and the Sun. For BML5, the $CS(3 \to 2)$ line is weak and the wings are probably lost in the

Fig. 15.— FIGURE NOT INCLUDED IN TEX FILE. SEE FILE f15.jpg. Grid of $CO(2 \to 1)$ spectra toward broad-molecular-line regions in W 28, with a spacing of 20". Within this 10×13 grid, W 28:BML4 is in Column 7, Row 8 (counting from the lower left). W 28:BML3 is in the upper left of this grid. OH 1720 MHz masers are at Maser (Column, Row): OHC2 (10,12), OHD2 (5,5), OHD3 (5,4) (Claussen et al. 1997).

noise.

The mm-wave line ratios for the W 28:BML1–BML5 are generally similar to each other: $CS(2 \to 1)/CO(2 \to 1) \sim 0.04$, $CS(3 \to 2)/CS(2 \to 1) \sim 1.0$. In 3C 391:BML1, the CS lines weaker, relative to than $CO(2 \to 1)$, by a factor of 2, but the ratio $CS(3 \to 2)/CS(2 \to 1)$ is similar, suggesting similar excitation conditions of $T_k \sim 100$ K and $n(H_2) \sim 10^5$ cm⁻³ (Reach & Rho 1996). The abundances of CS and HCO⁺ are similar to those found in 3C 391 and IC 443 (Ziurys et al. 1989) to within a factor of 3.

The SiO(2 \rightarrow 1) line was detected toward W 28:BML1: Figure 17 shows the spectrum and Table 2 shows the line fit. While the emission is weak, the SiO line profile is similar to other molecular transitions observed toward the same position. Of the other positions observed in this line, neither W 44:OHB nor W 44:OHF were detected, with $T_A^* < 0.12$ K. Because Si is locked in grains in quiescent interstellar gas, the presence of Si in the gas phase indicates either grain destruction or advanced grain-surface chemistry. Ziurys et al. (1989) detected SiO toward IC 443 and argued that the gas responsible for it has strongly enhanced SiO abundance, $100\times$ the upper limits of SiO abundance in dark clouds. Schilke et al. (1997) modeled the production of SiO in shocks and showed that the abundance is strongly enhanced by Si liberated from the shocked grain mantles and reacting with other molecules in the post-shock gas. To get the SiO line brightness we observed requires that the shocks are faster than 20 km s⁻¹, consistent with the observed line width of 21 km s⁻¹ (representing a lower limit to the shock velocity). Gas-phase Si was also detected in the far-infrared spectra of both W 28 and W 44, through the 34.8 μ m fine-structure line of Si⁺ (Reach & Rho 2000).

4.2. Near-infrared results for W 28

Let us now inspect the near-infrared image. The eastern portion of W 28 (Fig. 18) contains the brightest H₂ emission we observed in either remnant. There are large-scale H₂ arc complexes, one in the southeast and one in the northeast. The southeast large-scale arc is a very bright spur running from the easternmost portion of the arc toward the northwest. The bright bars contain the broad-molecular-line regions W 28:BML2 (brighter bar running diagonally SE/NW) and W 28:BML4 (upper bar running more N/S); these bright, broad,

Fig. 16.— FIGURE NOT INCLUDED IN TEX FILE. SEE FILE f16.jpg. Spectra of (a) W 28:BML2, (b) W 28:BML3, (c) W 28:BML4, and (d) W 28:BML5 in the $CO(2 \rightarrow 1)$ (top), $CS(2 \rightarrow 1)$ (middle), and $CS(3 \rightarrow 2)$ (bottom) lines.

Table 2: Broad Molecular Line regions in W 28

RA	Dec	$\int T_{mb}dv$	$\langle V \rangle$	ΔV	
(2000	0)	$(K \text{ km s}^{-1})$	$({\rm km~s^{-1}})$	$({\rm km~s^{-1}})$	line
W 28:BML1					
18:01:52.0	-23:18:47	466	11.7	21.3	$CO(2 \rightarrow 1)$
		19	4.3	18.2	$CS(2 \to 1)$
		33	3.6	28.8	$HCO^+(1 \to 0)$
		3.2	9.6	21.9	$SiO(2 \to 1)$
W 28:BML2					
18:01:37.4	-23:25:44	970	7.1	18.9	$CO(2 \to 1)$
		-21	8.0	1.5	$CO(2 \rightarrow 1)$ absorption
		36	6.6	12.1	$CS(2 \to 1)$
		37	6.6	15.6	$CS(3 \to 2)$
W 28:BML3					
18:01:44.1	-23:24:24	422	9.1	17.1	$CO(2 \to 1)$ broad
		100	5.8	3.8	$CO(2 \to 1)$ narrow
		14	7.5	8.9	$CS(2 \to 1)$ broad
		8	6.1	2.4	$CS(2 \to 1)$ narrow
		14	7.5	8.9	$CS(3 \rightarrow 2)$ broad
		8	6.1	2.4	$CS(3 \rightarrow 2)$ narrow
W 28:BML4					
18:01:39.5	-23:25:04	1090	7.6	24.1	$CO(2 \to 1)$
		-29	7.6	1.2	$CO(2 \rightarrow 1)$ absorption
		43	7.6	15.6	$CS(2 \to 1)$
		41	7.3	15.0	$CS(3 \to 2)$
W 28:BML5					
18:01:38.8	-23:29:03	840	2.4	30.4	$CO(2 \to 1)$
		25	5.5	29.2	$CS(2 \to 1)$
		17	5.4	11.1:	$CS(3 \to 2)$

Fig. 17.— FIGURE NOT INCLUDED IN TEX FILE. SEE FILE f17.jpg. Spectra of SiO emission from W 28:BML1, taken with the IRAM 30-m. This spectrum combines 30 minutes of on-source integration. The spectra of 3 other molecules toward the same position (and smoothed to the same angular resolution) are shown for comparison.

linear features have an average surface brightness of $10^{-3}~{\rm erg}~{\rm cm}^{-2}~{\rm s}^{-1}~{\rm sr}^{-1}$.

Fainter H_2 arcs are distributed throughout the region, generally along and parallel to the radio ridge, which comprises a north-south bar that turns roughly at a right angle into an east-west part at the location of the northeastern H_2 arc. The northeastern and southeastern H_2 arcs are connected by fainter emission; as a whole this H_2 ridge runs almost exactly parallel to the ridge of CO wing emission in Figure 13(g). The CO wing region W 28:BML1 is located just west of a relatively bright H_2 filament in the northeastern arc; this filament is probably due to a single, bright, edge-on shock propagating into a dense molecular core.

Fig. 18.— FIGURE NOT INCLUDED IN TEX FILE. SEE FILE f18.jpg. H_2 2.12 μ m image of the eastern portion of W 28.

The northern radio ridge, which runs east-west across the region covered by Figure 18, about 1/3 of the way from the top, contains the ridge of shocked $CO(3 \rightarrow 2)$ emission that was detected by Arikawa et al. (1999). There are some thin H_2 filaments that probably represent edge-on shocks. A pair of bright, nearly parallel filaments bracket a bright star near the junction between the north-south and east-west radio ridges. There are at least 3 shock fronts at this individual location.

5. Discussion

5.1. Correlation between the shocked CO and H_2

The clumpy H_2 emission is spatially associated with the broad-line CO emission. Examples of this are in the southern part of W 44, where the bright elliptical region of H_2 emission (Fig. 9) corresponds to the broad-line CO-emitting region near W 44:OH B (Fig. 7). Also the bright H_2 emission in W 28 exists in the region of broad CO lines; Figure 19 shows the CO overlaid on the H_2 image. The correspondence between H_2 and CO is not perfect, but the overall location of the CO and H_2 are similar and some features agree in detail. In particular, the bright CO bars in the southern portion of the image are both associated with H_2 . Individual H_2 filaments are narrow (~ 1 to 2"), so they are highly diluted in the CO beam (30") and may be detected with better angular resolution or sensitivity.

A good correspondence between H_2 and broad CO was seen for IC 443 (Burton et al. 1988; Rho et al. 2001). Such correspondence was also seen in 3C 391, where the H_2 broke into clumps that are likely pre-existing dense cores in the parent molecular cloud (Reach & Rho 2000). Such condensations are expected in star-forming clouds such as the parent clouds of W 28 and W 44. Since the progenitors of W 28 and W 44 were massive stars, forming rapidly and existing as stars briefly, it is like that there is continuing formation of lower-mass stars from the same clouds, in accordance with the initial mass function (Scalo 1986). The blast waves from the W 28 and W 44 progenitors are propagating into these environments, which span a range of densities. The volume density inferred from the CO excitation discussed above, and from the detection of far-infrared H_2O , OH, and high-J CO lines (Reach & Rho 1998), is $n_C > 10^5$ cm³. Pre-stellar cores have significant regions with density $\sim 10^5$ cm⁻³ on a timescale $\sim 10^5$ yr (André, Ward-Thompson, & Barsony 2000). Shocks into these regions will be non-dissociative, and the H_2 emission arises from collisionally-heated molecules behind the shock (Draine et al. 1983).

Fig. 19.— FIGURE NOT INCLUDED IN TEX FILE. SEE FILE f19.jpg. Overlay of CO emission (thin contours) on the H₂ image (greyscale) of the eastern portion of W 28. The region observed in CO is bounded by the thick bounding box. Small squares indicate the locations of OH 1720 MHz masers.

5.2. Physical properties of the shocked CO

The CO observations clearly differentiate between the shocked and unshocked gas. In addition to the broad line profile, the brightness ratios among the various spectral lines is different in the shocked gas as compared to the ambient gas. This is because the shocked gas is warmer (and often denser) than the unshocked gas, so that the relative brightness of shocked gas is higher in $CO(2 \to 1)$ than in $CO(1 \to 0)$. Figure 20 illustrates this clearly. The narrow component is present in both spectral lines, with identical width. The brightness ratio $R_{21} \equiv W[CO(2-1)]/W[CO(1-0)] = 0.7 \pm 0.1$, using the line integral of gaussian fits to the narrow component. The line ratio for the ambient gas is typical for molecular clouds in the inner galaxy, where for example a value of 0.74 ± 0.02 was observed for clouds in the Galactic center region, and 0.77 and 0.66 were observed for two giant molecular clouds in Orion, consistent with cold, optically thick gas, for example $T \sim 10$ and $n \sim 10^3$ cm⁻³ (Oka et al. 1996; Sakamoto et al. 1994).

The broad component is much fainter in $CO(1 \rightarrow 0)$ than in $CO(2 \rightarrow 1)$: $R_{21} = 3.5 \pm 0.9$, using the line integral over -20 to +65 km s⁻¹ after subtracting the narrow component. The line ratio R_{21} for the shocked gas is much higher than that of ambient molecular gas, due to a combination of heating and compression. A similarly high R_{21} was seen for the shocked gas in HB 21 (Koo et al. 2001) and IC 443 (Seta et al. 1998). That the line ratios are different is not surprising, if the broad line arises from molecules surviving a C-type shock while the narrow line is mostly ambient, unshocked gas. The utility of $CO(2 \rightarrow 1)/CO(1 \rightarrow 0)$ as a tracer of shocked gas has also been discussed by Seta et al. (1998). The actual line ratio could be even higher in the shocked gas, if there is significant structure on angular scales smaller than the beam—which is likely, given the fine-scale structure of the shocked H₂ images—so it is clear that there is a dramatic difference between the properties of the shocked and ambient gas.

Fig. 20.— FIGURE NOT INCLUDED IN TEX FILE. SEE FILE f20.jpg. Spectra of $CO(2 \to 1)$ [solid line] and $CO(1 \to 0)$ [dashed line, scaled by a factor of 0.5] averaged over the portions of the W 44 (0.4 arcmin²) with the most prominent broad molecular line wings. It is clear that the line wings are much more prominent in the $2 \to 1$ line, while the narrow component is essentially identical in the two lines.

We can constrain the physical properties of the broad-line emitting gas using R_{21} and the isotopic brightness ratio $R_{13/12} \equiv W[^{13}CO(1 \rightarrow 0)]/W[^{12}CO(1 \rightarrow 0)]$. From Figure 5, the upper limit to the brightness of $^{13}CO(1 \rightarrow 0)$ is 2% of the brightness of $^{13}CO(2 \rightarrow 1)$, which converts, using $R_{21} = 3.5$, to a brightness ratio $R_{13/12} < 0.07$. Assuming an isotopic ratio of $^{13}CO/^{12}CO=50$ (Wilson and Rood 1994), the upper limit to the optical depth is

 τ [CO(1 \to 0)] < 3. Using the optically thin limit, and balancing collisions and radiative transitions for the lowest several levels of CO, we find that the temperature of the shocked CO \sim 100 K, independent of density, and a lower limit to the density is $n({\rm H}_2) > 4 \times 10^3$ cm⁻³.

An independent estimate of the properties can be obtained from the CS observations. For lines of sight with detected CS(3 \rightarrow 2) and CS(2 \rightarrow 1), we measure $R_{32}^{CS} \equiv W[CS(3 \rightarrow 2)]/W[CS(2 \rightarrow 1)] \simeq 1$ (Table 2), which requires high volume densities, $n(H_2) > 9 \times 10^4$ cm⁻³ for $T \lesssim 100$ K.

The CO and CS line ratios can be explained by gas with $n(\mathrm{H}_2) = 2 \times 10^5$ cm⁻³ and T = 100 K, which are the conditions we inferred from a multi-level analysis of CS lines from the shocked gas in in 3C 391, where the $\mathrm{CS}(5 \to 4)$ line was also observed (Reach & Rho 1999). It is clear that the broad emission lines are due to warm gas, heated by the shock. This is important because fast shocks, with $v_s > 40$ km s⁻¹ dissociate H₂ molecules (Draine and McKee 1993). The width of the broad molecular lines, ~ 20 km s⁻¹, is probably indicative of the velocity of the shocks it experiencing. Warm, broad-line gas is most easily explained by non-dissociative shocks (Draine et al. 1983).

5.3. Relationship of OH masers to shocked CO and H₂

Many shock-excited OH 1720 MHz masers are located within W 44 and W 28. All of the OH masers are located in or near H₂ emission, and all of the masers are in or near broad CO emission. This clearly supports the idea that OH masers are signposts of interaction between supernova remnants and molecular clouds (Frail & Mitchell 1998). But the H₂ and CO images are far from a one-to-one correspondence with OH masers: many locations of bright H₂ have no OH masers, and the CO and H₂ peaks only rarely coincide with masers.

Figure 19 compares the locations of 33 OH masers (Claussen et al. 1997) in W 28 with the H₂ and CO images. The OH masers closely trace one of the filaments of H₂ emission, in the northeast. This is not the brightest H₂ filament, nor is it obviously special in any other way. But the conditions within this filament—its viewing geometry, or its location with respect to the bright radio synchrotron emission that the maser can amplify—are evidently much better for creating maser emission that other, comparable portions of the remnant. Examples of regions where OH masers lie along H₂ filaments are seen in the northeast portion and souther portion (Fig. 24) of W 44 as well. The spatial alignments are too detailed to be coincidence. Counterexamples of similar filaments with no OH masers, or OH masers not located on bright H₂ filaments, are present throughout both remnants. Wherever there

are OH masers, though, there is H_2 emission. Thus it appears that OH masers are a very non-linear tracer of shocked molecular gas. The presence of OH masers clearly indicates molecular shocks, but a lack of OH masers is not informative.

5.4. Shock thickness

The H_2 images of W 28 and W 44 reveal bright, complex regions as well as a network of fainter, narrow filaments. Figure 21 shows an example of a region with many narrow filaments. The individual shock fronts in W 28 and W 44 are barely resolved in the near-infrared H_2 images, with angular widths $\lesssim 0.7$ –4". If they are interpreted as edge-on shock fronts, then we are observing shock fronts with thicknesses of 3–12 × 10¹⁶ cm. This is really an upper limit, because the narrowest shocks are unresolved at the limit of atmospheric seeing, and all of these shocks have some inclination with respect to the line of sight. In what follows, we compare the shock thickness to theoretical models for non-dissociative and dissociative shocks.

The observed widths agree with the predictions for noon-dissociative shocks with properties as were invoked above to explain other properties of the gas (CO and CS line ratios). From equation 3.12 of Draine and McKee (1993), using a preshock magnetic field strength of $bn^{1/2}$ μ G where n is the preshock gas density in cm⁻³ and b is a dimensionless field strength of order unity, the shock thickness

$$L \sim 1.3 \times 10^{16} b(10^{-4}/x)(10^2/n) \text{ cm},$$

where $x = n_i/n$ and n_i is the ion density. For preshock gas densities between $n = 10^2$ and 10^4 cm⁻³ and corresponding ionization fractions between $x = 10^{-4}$ and 10^{-7} , respectively, the shock thickness is in the range $1-10 \times 10^{16}$ cm. Draine et al. (1983), in Figs. 1–2 of their paper, predict the structures of of 25 km s⁻¹ shocks into gas with pre-shock H-nucleon density 10^2 and 10^4 cm⁻³. The width of the region where H₂ would be heated, but not converted into more complex molecules like H₂O, is smaller than the total shock thickness estimated by the equations above: reading from their figures, the H₂ emission regions are $\sim 1 \times 10^{16}$ cm. The observed widths of the shock fronts are consistent with non-dissociative shocks into gas with densities of order 10^4 cm⁻³. Shocks into gas with pre-shock density 10^6 cm⁻³ (if they are steady shocks, which may not occur on the timescales of the remnants we are observing) are predicted to be wider than observed, and Figure 3 of Draine et al. (1983) shows most of the cooling will come from coolants other than H₂.

Faster, dissociative shocks, can also produce H_2 emission from molecules reforming behind the shock. Hollenbach & McKee (1989) calculated the width of the H_2 reformation region to be (their equation 3.4)

$$5 \times 10^{17} b(100/n) [1 + 100e^{-(6 \times 10^6/n)^{0.2}}] \text{ cm},$$

for a shock speed of 100 km s⁻¹, as was inferred from the width of the O I 63 μ m emission line (Reach & Rho 2000). The observed shock thickness can be produced if the density $n \sim 10^3$ cm⁻³. Thus, based only on the observed thickness, there are two types of shock that can produce structures with the thickness observed: non-dissociative shocks into gas with density $\gtrsim 10^4$ cm⁻³ and dissociative shocks into gas with density $\sim 10^3$ cm⁻³.

5.5. Relation between molecular and ionic shocks

Portions of the remnants were observed in the Fe II 1.644 μ m filter. While the H_2 emission is bright and extended, with intricate filaments as well as bright blobs, the Fe II emission is weak and relatively diffuse. Figure 22 shows the Fe II image of the southern portion of W 44, revealing two diagonal filaments, qualitatively similar to the H₂ image (Fig. 9) but with the Fe II filaments much more diffuse and shifted north of the H₂ filaments. The separation of the Fe II and H₂ emission is not particularly surprising, considering that the physical conditions of the shocks traced by these lines is very different. However, the rough alignment of the filaments and the fact that they are offset in the direction toward the center of the remnant is very suggestive. We might expect that a fast shock hitting the surface of a moderately-dense molecular cloud would produce Fe II, from the destroyed grains, as was seen in IC 443 (Rho et al. 2001) and 3C 391 (Reach et al. 2002). Then it is conceivable that the H₂ would be reformed molecules behind the shock, as was predicted theoretically by Hollenbach & McKee (1989) and tentatively observed in one remnant by Koo & Moon (1997). However, the H₂ emission in this image of W 44 is located further from the remnant center than the Fe II emitting region, whereas reformed molecules should be behind the shock. The observed separation between the molecular and ionic shocks is 2×10^{18} cm, which is much larger than the expected size of the molecular reformation region behind a fast shock: for $n_0=10^3~{\rm cm}^{-3}$ and $v_s=100~{\rm km~s}^{-1},\,z_{1/2}\simeq 10^{16}~{\rm cm}$ (Hollenbach & McKee 1989). The Fe II traces a combination of grain destruction (to get Fe in the gas phase) and hot and dense regions (to excite the upper energy levels). It is unlikely that the Fe II emitting region could end up further behind the shock than the H₂ emission.

Fig. 21.— FIGURE NOT INCLUDED IN ASTRO-PH SUBMISSION. SEE ApJ ARTICLE Blow-up of a portion of the northeastern rim of W 44 in the 2.12 μ m H₂ line. The region depicted occupies the lower portion of Fig. 8; it is outlined as a dashed rectangle, labeled Fig21, in Fig. 2.

Therefore, we interpret the Fe II and $\rm H_2$ filaments as tracing independent shocks: the Fe II traces fast, grain-destroying shocks into $n < 10^3$ cm⁻³ gas, while the $\rm H_2$ traces denser shocks. The reason for their rough correspondence and occasional parallel alignment on the sky is probably reflective of the pre-shock structure of the molecular cloud. When approaching a dense portion of the molecular cloud, the blast wave first encounters the less-dense material at its surface yielding the ionic shocks. Slower shocks then begin propagating into the denser material, yielding the molecular shocks.

5.6. Shock brightness

The H_2 $(1 \rightarrow 0)$ S(1) line brightness of the individual, filamentary shock fronts in Figure 21 is about 5×10^{-5} erg s⁻¹ cm⁻² sr⁻¹. Brighter features, such as the bright clump in Figure 9, range up to 2×10^{-4} erg s⁻¹ cm⁻² sr⁻¹. Let us compare these values to those predicted by shock models consistent with other observed properties. The predicted face-on brightness of nondissociative shock fronts into $n = 10^4$ cm⁻³ and $V_s = 25$ km s⁻¹ is $\sim 3 \times 10^{-5}$ erg s⁻¹ cm⁻² sr⁻¹ (Draine et al. 1983), and the predicted face-on brightness of dissociative, J-shocks into $n = 10^3$ cm⁻³ and $V_s = 100$ km s⁻¹ is $\sim 2 \times 10^{-5}$ erg s⁻¹ cm⁻² sr⁻¹ (Hollenbach & McKee 1989). Both of these predictions are comparable to, but a factor of 2–3 fainter than, the brightness of the individual, filamentary shock fronts. The theoretical models are for face-on shocks, which are fainter than edge-on shocks. It is quite plausible for there to be a factor of 2–3 geometric correction between face-on (theoretical) and more nearly edge-on (observed) geometries. It is a rather remarkable coincidence that both the thickness and brightness of the near-infrared H_2 emission, from two very different types of shocks, is so similar.

There is a significant difference in the physical properties of H_2 behind the different shocks. Behind a non-dissociative, C-type shock, the H_2 molecules are heated without being dissociated; there must exist a critical type of shock that can just barely dissociate H_2 that will yield the highest possible excitation. The neutral gas temperature behind such shocks reaches 10^3 K then cools rapidly, leading to bright emission from the S(3) and S(5) pure rotational lines (Draine et al. 1983). In contrast, behind a faster shock, the H_2 molecules are destroyed and the H ionized; the molecules reform $\sim 10^{17}$ cm behind the shock where the temperature is $10^{2.5}$ K and lower. The cooling is somewhat slower because of the lower

Fig. 22.— FIGURE NOT INCLUDED IN TEX FILE. SEE FILE f22.jpg. ionFe2 1.644 μ m image of the southern portion of W 44. This is a subfield of the region covered by the H₂ image in Figure 9; the location in the remnant is indicated in Figure 2.

density, leading to bright emission from from the S(7) and S(9) pure rotational lines (Hollenbach & McKee 1989). Let us now take models consistent with the observed near-infrared 1–0 S(1) line brightness and consider the Infrared Space Observatory data on the pure rotational lines. For one line of sight each in remnant, near W 28:OHF and W 44:OHE, we detected the S(3) and S(9) lines in the $14'' \times 20''$ spectrometer aperture (Reach & Rho 2000). The ratios S(9)/S(3) are 0.1 and 0.5 for W 28:OHF and W 44:OHE, respectively, with < 10% uncertainties. The predicted line ratios are S(9)/S(3)=10 for the dissociative shock and S(9)/S(3)=0.02 for the non-dissociative shock. The observed line ratio is inconsistent with both shock models, so we infer that there must be different types of shock producing different lines. Using the theoretically predicted ratios of the S(3) and S(9) lines, the S(3) line arises almost exclusively from the non-dissociative shock (> 94 \%), while the S(9) line arises largely from the dissociative shock (> 83 \%). Thus both types of shock are expected to contribute to the near-infrared H₂ emission with comparable brightness averaged over large beams.

To separate between the dissociative and non-dissociative shocks, we must turn to evidence other than the shock width and brightness. The filamentary H_2 emission is unlikely to arise from very dense cores $(n_0 > 10^4 \text{ cm}^{-3})$, because the filaments are coherent and long (> 2 pc). If the filamentary H_2 emission is from a shock front propagating into a coherent three-dimensional region with this size and density, the pre-shock gas would have a mass $\gg 10^4 M_{\odot}$ and would have been easily visible in the millimeter-wave lines that trace such gas. In fact, the $CS(2 \to 1)$ spectra do not show such large-scale dense material, revealing instead only relatively isolated cores with much smaller size. The distribution of pre-shock molecular gas is complicated, and the new images of shock fronts propagating into giant molecular clouds presented in this paper deserve more complicated theoretical models to elucidate both the shock physics and pre-shock gas distribution.

5.7. Molecular shocks and cosmic rays

Supernova remnants are the most plausible source for galactic cosmic rays (Draine and McKee 1993; Jones and Ellison 1991). Most attention has been focused on young supernova remnants, where the shocks are strong enough to accelerate thermal electrons to relativistic energies. W 28 and W 44 are very bright radio continuum sources (Clark and Caswell 1976); they are the 6^{th} and 7^{th} brightest supernova remnants out of 232 remnants in the Green catalog. The synchrotron radiation could be bright for several reasons: the strength of the magnetic field in the dense material with which the blast waves are interacting, local acceleration of particles to high energies, re-acceleration of existing high-energy particles, or some combination of these effects. Particle acceleration (or reacceleration) will depend on the

physical conditions of the pre-shock gas and the strength of the shock.

If all the present-day shocks into different regions are being driven by the same ram pressure, then we can discern which types of pre-shock gas are the most likely origin for particle acceleration or re-acceleration by comparing images that trace the various types of shock to the radio image. For young remnants, the radio and X-ray images sometimes show very close correspondence—for example the images of Tycho compared by Blandford and Cowie (1982), or the near-infrared synchrotron, radio, and X-ray images of Cas A compared by Rho et al. (2003)—so the cosmic ray acceleration is associated with the main blast wave. But for mixed-morphology remnants like W 28 and W 44, whose defining characteristic is the contrasting X-ray and radio morphology, we must look to shocks that do *not* emit copious X-rays to find the source of cosmic ray acceleration.

First, let us compare the $H\alpha$ and radio images. We assume that the near-infrared H_2 emission and broad CO emission trace shocks into dense gas (> 10^3 cm⁻³), and the H α image traces shocks into lower-density gas $(n_A \sim 5 \text{ cm}^{-3})$. Figure 23 shows that the radio image is quite different from $H\alpha$ for W 28, with the radio shell surrounding the centrally-filled $H\alpha$ emission. This morphology was already noted by Van den Bergh, Marscher, & Terzian (1973). Some faint H α emission is associated with the outer radio shell, for example along the northernmost radio arc and the northwestern portion of the remnant (Dubner et al. 2000). But the vast majority of the H α emission arises from the interior of the remnant, where the radio emission is very weak. In particular, the brightest radio emission arises from a very bright bar that runs north-south and forms the eastern boundary of the remnant. The H α emission fills the interior of the remnant and ends abruptly at the radio bar. The secondbrightest radio feature is a bar that runs east-west in the northern part of the remnant. The bright $H\alpha$ emission in the interior again terminates at this radio bar as well. The third-brightest radio feature is a thin arc of fainter emission that forms the far northern boundary of the remnant; this is where some faint $H\alpha$ emission appears associated with the radio emission. Thus it appears that, for the most part, the inner boundary of the radio shell delineates the outer boundary of the H α emitting region. The morphology of the radio and $H\alpha$ emitting regions is also different: while the radio can be described as a set of large, coherent arcs running along the edge of the remnant, the $H\alpha$ emission is highly structured with many very thin filaments, some of which run orthogonal to the radio arcs. The difference in fine structure is difficult to assess with the present data, however, because their angular resolution of the radio data is much lower than that of the H α . Similar results obtain for W 44, though the H α emission is weaker. Rho et al. (1994) showed that the H α emission is interior to the radio shell and has different morphology. Giacani et al. (1997) showed that there are some portions of the W 44 where the H α and [S II] appear to follow each other and the radio, though there is also optical emission from regions with no corresponding radio emission. The situation for both W 28 and W 44 is that some regions have corresponding $H\alpha$ and radio emission, but for the most part (and especially in the interior of the remnant), the radio and optical images are very different.

Next, let us compare the H_2 and radio images. Figure 24 shows radio contours overlaid on the H_2 image of the southern portion of W 44. Both images are dominated by two diagonal filaments running SE-NW across the field. The orientation of the filaments matches remarkably well in these two images of disparate emission mechanisms. The radio emission from the southernmost of the two bright filaments overlays the H_2 filament very closely. Even the relatively faint radio and H_2 features have very good correspondence, throughout this image.

The brightest patch of H₂ emission, which is just south of the northern filament in Figure 24 and contains the W 44:OHB maser complex, has a faint radio counterpart of about 1.5 mJy/beam brightness. The radio/H₂ ratio is at 3 times less in the H₂ clump than in the H₂ filaments. The shocks into the highest-density gas, traced by the 'clumpy' type of H₂ emission (as opposed to the long, thin filaments), OH masers, and wide CO lines, has apparently a lower synchrotron emissivity than the filaments.

For W 28, a similar correspondence is found between H_2 and radio emission, though the angular resolution of the radio image is much worse. The bright H_2 emission in the SE portion of Figure 18 is precisely where the radio emission in the remnant is brightest in its north-south bar. The shocked CO emission was shown to be well correlated with the radio image by Arikawa et al. (1999) and (Dubner et al. 2000).

Because the radio and shocked molecular filaments are well correlated, we suggest that the bright radio emission from W 28 and W 44 is due to interaction between the remnant and molecular gas. Such an association is somewhat surprising, because it would seem that the fastest shocks would be most closely associated with energetic particle acceleration. But strong magnetic fields in dense gas, and the presence of stronger shocks into the lower density gas, combine to provide the particle acceleration and synchrotron enhancement, respectively.

Fig. 23.— FIGURE NOT INCLUDED IN TEX FILE. SEE FILE f23.jpg. Overlay of radio contours onto the H α image (greyscale) for W 28. The very bright black spot in the upper left corner is the Trifid Nebula. The radio contours surround the H α emission from W 28, which is the box-shaped region in the center of the image. The H α image suffers from some extinction. In particular, there is a thick band running diagonally NE-SW that appears in extinction both in the H α and red continuum images. The radio contours range from 0.1 to 1 mJy/beam in 12 equal steps.

Bykov et al. (2000) has addressed this issue theoretically. The present-day shocks in W 28 and W 44 may not be strong enough to be primary accelerators of cosmic rays, though fast shock fronts are capable of accelerating thermal electrons to relativistic energies (Jones and Ellison 1991). What we observe as enhanced radio emission is relativistic particles that emit bright synchrotron radiation as they spiral around the strong magnetic field in the compressed regions behind the molecular shocks. This mechanism was proposed by Blandford and Cowie (1982). For a remnant of given explosion energy and present size, the radio surface brightness depends primarily on the filling factor, f, of dense material behind the shock: $\Sigma \propto B^{-0.3} f$, where B is the magnetic field in the dense gas. The radio map is therefore predicted to trace the dense gas, as is indeed observed in Figure 24. Quantitatively, the radio brightness of W 44 ranges from 3-10 MJy sr^{-1} (where 1 MJy = 10^{-17} erg s^{-1} cm⁻² Hz⁻¹) at 1420 MHz. The observed brightness is somewhat higher than the model predictions, even for a high filling factor of dense gas; this is not surprising because the model assumes a low filling factor and neglects the effect of the high density on the remnant evolution, which becomes important at higher filling factors. Thus our new observations appear to confirm the concept proposed by Blandford and Cowie (1982).

Based on far-infrared and millimeter-wave spectroscopy, we have suggested there are three types of gas that produce the main observable features of supernova remnants interacting with molecular clouds (Reach & Rho 2000). Table 5.7 describes the physical properties of these three types of gas. The three types, i, of gas with density n_i , shock velocity V_i , and filling factor f_i , will contribute to the synchrotron emission proportional to $n_i^{1.75}V_if_i$, assuming magnetic field $B_i \propto n_i^{0.5}$. The kinetic energy in their shocks is proportional to $p_{ram,i}f_i \propto n_iV_i^2f_i$. The filling factors in Table 5.7 are very rough approximations based on the fraction of remnant surface that is traced by each phase. The ram pressure of shocks into the different phases is similar but not equal: the observed properties of the denser shocks seem to require higher ram pressure (Reach & Rho 1996). This effect may have been theoretically explained by Chevalier (1999). The radio emission arises from the intermediate-density molecular phase, in agreement with our finding that the H₂ and radio images are associated. Phase M dominates the mass, although phase A contains the most kinetic energy.

Fig. 24.— FIGURE NOT INCLUDED IN TEX FILE. SEE FILE f24.jpg. Overlay of radio contours onto the H_2 image (greyscale) for a $10.1' \times 11.7'$ in the southern portion of W 44; (the same region in Figs. 9 and 10). Contours are evenly spaced from 0.3 to 2.5 mJy/beam. The radio image was spatially filtered by subtracting a version smoothed to 4', which removes the diffuse emission (which has a brightness of 1.5 mJy/beam over most of the field). The radio beam size is 15". Squares denote the positions of OH 1720 MHz masers, and the ' \times ' indicates the position of the pulsar B1853+01.

Table 3. Three types of shocks in molecular clouds $\,$

	Atomic	Molecular	Clump						
A.	Properties of the pre-s	shock gas:							
description	atomic, inter-clump	molecular	clump, core						
tracer	ΗI	low-J CO	CS, protostars						
density, n_0	5	200	2×10^4	(cm^{-3})					
fill factor, f	0.9	0.1	10^{-4}						
mass	800	5000	300	(M_{\odot})					
B. Ob	B. Observed properties of the shocked gas:								
description	shell	filaments	clumps						
tracer	radio, X-ray	radio, [O $ m I$], $ m H_2$	H ₂ , broad molecular lines						
velocity, V_S	500	100	25	$({\rm km}\ {\rm s}^{-1})$					
ram pressure, p_{ram}	3	5	20	$(10^{-8} \text{ dyne cm}^{-2})$					
energy, E_{kin}	4	1	0.005	(10^{51} erg)					
density	20	3×10^3	2×10^5	(cm^{-3})					
$synchrotron^a$	0.01	0.7	0.3						
C. Theor	retical expectations for	the shocked gas:							
shock type	very fast	dissociative	magnetohydrodynamic						
main coolant	metastable lines	fine structure lines, grains	molecular lines						
$I[H_21-0 S(1)]$		3×10^{-5}	2×10^{-5}	${\rm erg}~{\rm s}^{-1}~{\rm cm}^{-2}~{\rm sr}^{-1}$					
$H_2 S(3)/1-0 S(1)$	•••	0.5	150						
$H_2 S(9)/1-0 S(1)$		4	2						
$I[{ m O~I,63}\mu{ m m}]$	1×10^{-4}	1×10^{-3}	1×10^{-5}	${\rm erg}~{\rm s}^{-1}~{\rm cm}^{-2}~{\rm sr}^{-1}$					

 $^{^{\}rm a}{\rm Fraction}$ of synchrotron emission produced be each type of gas.

There is another possible source of energetic particles, at least for W 44: the pulsar PSR 1853+01. The pulsar is located just north of Figure 24, and the distance from the pulsar to the northern radio filament is only $\sim 10^{18}$ cm. The radio filaments in W 44 seem to converge in the southwest portion of the remnant, and we speculate that that energetic particles could originate from the pulsar wind then spiral along the filaments of enhanced magnetic field. de Jager and Mastichiadis (1997) also proposed that the pulsar supplies the energetic particles, based on interpretation of the radio-to- γ -ray spectrum.

5.8. Implications for the structure of molecular clouds

We mentioned in the introduction that theoretical models (Cox et al. 1999; Chevalier 1999) for molecular supernova remnants explain most observable properties as shocks into gas with a density of 5 cm⁻³. These models are well grounded in observational data: in particular, H I 21-cm observations indicate neutral hydrogen shells containing $\sim 10^3~M_\odot$ of material, suggesting pre-shock densities $\sim 2-5~{\rm cm}^{-3}$ for W 28 (Velázquez et al. 2002) and W 44 (Koo & Heiles 1995). From our millimeter-wave and infrared observations, we have inferred shocks into gas with densities 10³ cm⁻³ or higher. How can these be reconciled? Molecular clouds comprise regions with a wide range of densities, from dense, star-forming cores with $n > 10^5$ cm⁻³ to CO-emitting regions with $n > 3 \times 10^2$ cm⁻³, and possibly lower if there is interclump gas. Detailed observations of molecular clouds have shown that CO emission is from regions with volume density n_M much higher than the path-length averaged density $\langle n \rangle \equiv N/L$. For a giant molecular cloud such as the ones near W 44 and W 28, $N \sim 2 \times 10^{22} \ {\rm cm^{-2}}$ and $L \sim 100 \ {\rm pc}$, so $\langle n \rangle \sim 10^2 \ {\rm cm^{-3}}$. A detailed study of the Rosette molecular cloud reveals that the CO emission arises from clumps that occupy only 8% of the cloud volume; the remainder of the cloud is filled with diffuse atomic gas with a mean density $n_A \sim 4 \text{ cm}^{-3}$ (Williams, Blitz, and Stark 1995). In a recent study of H I absorption toward a large sample of dark clouds, Li and Goldsmith (2003) showed pervasive atomic gas within molecular clouds, with a volume density $n(H I) \sim 4 \text{ cm}^{-3}$. They interpreted the H I as the product of cosmic-ray destruction of H₂ in dark clouds; since the H I volume density is predicted to be independent of the H₂ density, the H I can be thought of as an interclump medium in a clumpy cloud. There is increasing evidence that the bulk of the mass of molecular clouds resides in clumps that fill only a small fraction of the cloud. An IRAM key project demonstrated that CO emission arises from cells that do not fill the volume of the cloud, having densities 10³–10⁵ cm⁻³ and sizes of order 200 AU (Falgarone et al. 1998). Multi-level excitation studies show that even the $CO(4 \rightarrow 3)$ line is bright so that the fourth rotational level is excited; the inferred volume density $n_M \sim 10^{4.5} \ {\rm cm}^{-3}$ (Ingalls et al. 2000).

6. Conclusions

We have used supernova blast waves as a means of illuminating the cloud structure. Radiative shocks into gas of different densities have different cooling mechanisms, allowing us to separate shocks into dense cores, moderate-density molecular gas, and interclump atomic gas. Giant molecular clouds are pervaded by interclump gas with density ~ 5 cm⁻³, with moderate-density CO-emitting portions occupying $\sim 10\%$, and denser gas occupying yet smaller volume.

One of the defining characteristics of supernova remnants in the mixed-morphology class to which W 28 and W 44 belong is their centrally-condensed, thermal X-ray emission (Rho & Petre 1998). Two competing theoretical explanations for the presence of such a large amount of interior X-ray emitting gas involve evaporating clumps inside the remnant (White and Long 1991) and thermal conduction behind radiative shocks (Cox et al. 1999). We now suspect that both mechanisms are operating. The thermal conduction model explains some interior X-rays, assuming shocks into interclump gas with a density of 5 cm⁻³. But this model does not produce a central column density peak with very flat temperature profile, required to match the X-ray observations. The combination of the radiative shock into the interclump gas and evaporating material from the dense clumps that survive the shock may work in combination to produce the X-ray emitting material. A reservoir of dense material that can survive the initial blast wave is clearly present: it manifests itself through broad molecular line regions, bright H₂ clumps, and OH masers. The shocks into these clumps are much slower than the shock into the interclump gas, which leaves the clumps behind to evaporate in the interior. The variegated appearance of these two supernova remnants interacting with molecular clouds owes to the wide range of densities already present in the clouds, with fast shocks producing X-ray, $H\alpha$, and Fe II emission, slower shocks into moderate-density gas producing filamentary H₂, and radio emission, and slower-yet shocks into dense cores producing CO, CS, and HCO⁺ emission.

This work is based on observations obtained at the Hale Telescope, Palomar Observatory, as part of a continuing collaboration between the California Institute of Technology, NASA/JPL, and Cornell University. We are pleased to acknowledge the assistance of Naman Bhatt, who worked with us for a summer on this project. This publication makes use of data products from the Two Micron All Sky Survey, which is a joint project of the University of Massachusetts and the Infrared Processing and Analysis Center/California Institute of Technology, funded by the National Aeronautics and Space Administration and the National Science Foundation. Observations with the 12-meter telescope were made while that telescope was being operated by the National Radio Astronomy Observatory (NRAO). The

NRAO is a facility of the National Science Foundation, operated under cooperative agreement by Associated Universities, Inc. The research described in this paper was carried out at the California Institute of Technology under a contract with the National Aeronautics and Space Administration.

REFERENCES

- André, P., Ward-Thompson, D., & Barsony, M. 2000, in *Protostars and Planets IV*, eds. V. Mannings, A. P. Boss, & S. S. Russell (Tucson: University of Arizona Press), 59
- Arikawa, Y., Tatematsu, K., Sekimoto, Y., & Takahashi, T. 1999, PASJ, 51, L7
- Bitran et al. 1997, A & A S, 125, 99
- Blandford, R. D., and Cowie, L. L. 1982, ApJ, 260, 625
- Bloemen, J. B. G. M., Strong, A. W., Mayer-Hasselwander, H. A., Blitz, L., Cohen, R. S., Dame, T. M., Grabelsky, D. A., Thaddeus, P., Hermsen, W., & Lebrun, F. 1986, A&A, 154, 25
- Burton, M. G., Geballe, T. R., Brand, P. W. J. L., and Webster, A. S. 1988, MNRAS, 231, 617
- Burton, W. B. 1988, in *Galactic and Extragalactic Radio Astronomy*, eds. G. L. Verschuur and K. I. Kellermann (New York: Springer), p. 296
- Bykov, A. M., Chevalier, R. A., Ellison, D. C., Uvarov, Yu. A. 2000, ApJ, 538, 203
- Chevalier, R. A. 1999, ApJ, 511, 798
- Clark, D. H., and Caswell, J. L. 1976, MNRAS, 174, 267
- Claussen, M. J., Frail, D. A., Goss, W. M., & Gaume, R. A. 1997, ApJ, 489, 143
- Claussen, M. J., Goss, W. M., Frail, D. A., & Desai, K. 1999, ApJ, 522, 349
- Claussen, M. J., Goss, W. M., Desai, K. M., & Brogan, C. L. 2002, ApJ, 580, 909
- Cox, D. P., Shelton, R. L., Maciejewski, W., Smith, R. K., Plewa, T., Pawl, A., & Rózyczka, M. 1999, ApJ, 524, 179
- Dame, T. M., Elmegreen, B. G., Cohen, R. S., and Thaddeus, P. 1986, ApJ, 305, 892
- Dame, T. M., Hartmann, D., and Thaddeus, P. 2001, ApJ, 547, 792
- de Jager, O. C., and Mastichiadis, A. 1997, ApJ, 482, 874
- Denoyer, L. K. 1983, ApJ, 264, 141
- Dickel, J. R., Dickel, H. R., and Crutcher, R. M. 1976, PASP, 88, 840

- Draine, B. T., & McKee, C. F. 1993, ARA& A, 31, 373
- Draine, B. T., Roberge, W. G., & Dalgarno, A. 1983, ApJ, 264, 485
- Dubner, G. M., Velázquez, P. F., Goss, W. M., Holdaway, M. A. 2000, AJ, 120, 1933
- Esposito, J. A., Hunter, S. D., Kanbach, G., Sreekumar, P. 1996, ApJ, 461, 820
- Falgarone, E., Panis, J.-F., Heithausen, A., Perault, M., Stutzki, J., Puget, J.-L., & Bensch, F. 1998, A&A, 331, 669
- Frail, D. A., Goss, W. M., Slysh, V. I. 1994, ApJ, 424, L111
- Frail, D. A., Kassimn N. E., and Weilner K. W. 1994, AJ, 107, 1120
- Frail, D. A., Giacani, E. B., Goss, W. M., & Dubner, G. 1994, ApJ, 464, L165
- Frail, D. A., & Mitchell, G. F., ApJ, 508, 690
- Fryer, C. L. 1999, ApJ, 522, 413
- Giacani, E. B., Dubner, G. M., Kassim, N. E., Frail, D. A., Goss, W. M., Winkler, P. F., and Williams, B. F. 2001, AJ, 113, 1379
- Green D.A., 2001, 'A Catalogue of Galactic Supernova Remnants (2001 December version)', Mullard Radio Astronomy Observatory, Cavendish Laboratory, Cambridge, United Kingdom (available on the World-Wide-Web at http://www.mrao.cam.ac.uk/surveys/snrs/).
- Hartman, R. C., Bertsch, D. L., Bloom, S. D., Chen, A. W., Deines-Jones, P., Esposito, J. A., Fichtel, C. E., Friedlander, D. P., Hunter, S. D., McDonald, L. M., and 17 coauthors 1999, ApJS, 123, 79
- Hollenbach, D. J., and McKee, C. F. 1989, ApJ, 342, 306
- Ingalls, J. G., Bania, T. M., Lane, A. P., Rumitz, M., & Stark, A. A. 2000, ApJ, 535, 211
- Jones, A. P., Tielens, A. G. G. M., & Hollenbach, D. J. 1996, ApJ, 469, 740
- Jones, F. C., and Ellison, D. C. 1991, Space Sci. Rev., 48, 359
- Jones, L. R., Smith, A., Angellini, L. 1993, MNRAS, 265, 631
- Kaspi, V. M., Lyne, A. G., Manchester, R. N., Johnston, S., D'Amico, N. D., & Shemar, S. L. 1993, ApJ, 409, L57

Knapp, G. R., and Kerr, F. J. 1974, A&A, 33, 463

Koo, B,-C., and Heiles, C. 1995, ApJ, 442, 679

Koo, B.-C., & Moon, D.-S. 1997, ApJ, 485, 263

Koo, B.-C., Rho, J., Reach, W. T., Jung, J., & Mangum, J. G., ApJ, 552, 175

Li, D., and Goldsmith, P. F. 2003, ApJ, 585, 823

Liszt, H. and Lucas, R. 2000, A&A, 355, 333

Lockett, P., Gauthier, E., & Elitzur, M. 1999, ApJ, 511, 235

Long, K. S., Blair, W. P., Matsui, Y., White, R. L. 1991, ApJ, 373, 567

MacGillivray, H. T. 1998, PASA, 15, 42

Malin, D. 1998, PASA, 15, 38

Oka, T. Hasegawa, T., Handa, T., Hayashi, M., & Sakamoto, S. 1996, ApJ, 334, 342

Parker, Q. A., & Phillipps, S. PASA, 15, 28

Petre, R., Kuntz, K. D., & Shelton, R. L. 2002, ApJ, 579, 404

Reach, W. T., & Rho, J.-H. 1996, A& A, 315, L277

Reach, W. T., & Rho, J.-H. 1998, ApJ, 507, L93

Reach, W. T., & Rho, J.-H. 1999, ApJ, 511, 836

Reach, W. T., & Rho, J.-H. 2000, ApJ, 544, 843

Reach, W. T., Rho, J.-H., Jarrett, T. H., & Lagage, P.-O., 2002, ApJ, 564, 302

Rho, J., & Borkowski, K. J. 2002, ApJ, 575, 201

Rho, J., Petre, R., Schlegel, E. M., Hester, J. J. 1994, ApJ, 430, 757

Rho, J.-H., & Petre, R. 1998, ApJ, 503, L167

Rho, J., Jarrett, T., Cutri, R., & Reach, W. T. 2001, ApJ, 547, 885

Rho, J., Reynolds, S. P., Reach, W. T., Jarrett, T. H., Allen, G. E., & Wilson, J. C. 2003, ApJ, 529, 299 Rowell, G. P. et al. 2000, A&A, 359, 337

Sakamoto, S., Hayashi, M., Hasegawa, T., Handa, T., & Oka, T. 1994, ApJ, 425, 641

Scalo, J. M. 1985, Fund. Cosmic Phys., 11, 1

Schilkel, P., Walmsley, C. M., Pineau des Forêts, G., & Flower, D. R. 1997, A&A, 321, 293

Seta, M. et al. 1998, ApJ, 505, 286

Seta, M. Hasegawa, T., Sakamoto, S., Oka, T., Sawada, T., Insutsuka, S., Koyama, H., & Hayashi, M. 2004, AJ, 127, 1098

Seta, M. 1995, Ph. D. thesis, University of Tokyo

Shelton, R. L., Cox, D. P., Maciejewski, W., Smith, R. K., Plewa, T., Pawl, A., & Rózyczka, M. 1999, ApJ, 524, 192

Skrutskie, M. F. 1999, in *Astrophysics with Infrared Surveys: A Prelude to SIRTF*, eds. M. D. Bicay, C. A. Beichman, R. M. Cutri, & B. F. Madore (San Francisco: ASP), p. 185.

Spitzer, L. 1978, Physical Processes in the Interstellar Medium (New York: Wiley)

Van den Bergh, S., Marscher, A. P., & Terzian, Y. 1973, ApJS, 26, 19

Velázquez, P. F., Dubner, G. M., Goss, W. M., & Green, A. J. 2002, AJ, 124, 2151

Wardle, M., & Yusef-Zadeh, F. 2002, Science, 296, 2350

Wheeler, J. C. 1981, Rep. Prog. Phys., 44, 6

White, R. L., & Long, K. S. 1991, ApJ, 373, 543

Williams, J. P., Blitz, L., & Stark, A. A. 1995, ApJ, 451, 252

Wilner, D. J., Reynolds, S. P., & Moffett, D. A. 1998, AJ, 115, 247

Wilson, T. L., & Rood, R., 1994, ARA&A, 32, 191

Wolszczan, A., Cordes, J. M., & Dewey, R. J. 1991, ApJ, 372, L99

Woosley, S. E. 1987, in *The origin and evolution of neutron stars*, eds. D.J. Helfand and J.-H. Huang (Dordrecht: Reidel), 255

Wootten, H. A. 1977, ApJ, 216, 440

Wootten, A. 1981, ApJ, 245, 105

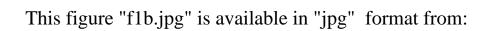
Yusef-Zadeh, F., Wardle, M., & Roberts, D. A. 2003, ApJ, 583, 267

Yusef-Zadeh, F., Wardle, M., Rho, J., & Sakano, M. 2003, ApJ, 585, 319

Ziurys, L. M., Snell, R. L., & Dickman, R. L. 1989, ApJ, 341, 857

This preprint was prepared with the AAS $\text{LAT}_{E\!X}$ macros v5.2.

This figure "fla.jpg" is available in "jpg" format from:



This figure "f2.jpg" is available in "jpg" format from:

This figure "f3.jpg" is available in "jpg" format from:

This figure "f4.jpg" is available in "jpg" format from:

This figure "f5.jpg" is available in "jpg" format from:

This figure "f6.jpg" is available in "jpg" format from:

This figure "f7.jpg" is available in "jpg" format from:

This figure "f8.jpg" is available in "jpg" format from:

This figure "f9.jpg" is available in "jpg" format from:

This figure "f11.jpg" is available in "jpg" format from:

This figure "f12.jpg" is available in "jpg" format from:

This figure "f13.jpg" is available in "jpg" format from:

This figure "f14.jpg" is available in "jpg" format from:

This figure "f15.jpg" is available in "jpg" format from:

This figure "f16.jpg" is available in "jpg" format from:

This figure "f17.jpg" is available in "jpg" format from:

This figure "f18.jpg" is available in "jpg" format from:

This figure "f19.jpg" is available in "jpg" format from:

This figure "f20.jpg" is available in "jpg" format from:

This figure "f22.jpg" is available in "jpg" format from:

This figure "f23.jpg" is available in "jpg" format from:

This figure "f24.jpg" is available in "jpg" format from: